UC Irvine
UC Irvine Previously Published Works

Title

Detecting lithium plating dynamics in a solid-state battery with operando X-ray computed tomography using machine learning

Permalink

https://escholarship.org/uc/item/0xk284wx

Journal

npj Computational Materials, 9(1)

ISSN

2057-3960

Authors

Huang, Ying

Perlmutter, David

Fei-Huei Su, Andrea

et al.

Publication Date

2023

DOI

10.1038/s41524-023-01039-y

Copyright Information

Peer reviewed

Detecting Lithium Plating Dynamics in a Solid-State Battery with *Operando* X-ray Computed Tomography using Machine Learning

Ying Huang[1†], David Perlmutter[2†], Andrea Fei-Huei Su[3], Jerome Quenum[2], Pavel Shevchenko[4], Dilworth Parkinson[5], Iryna V. Zenyuk[3*], Daniela Ushizima[2,6*]

[1] Department of Materials Science & Engineering, National Fuel Cell Research Center, University of California Irvine, California, USA
[2] Applied Math and Computational Research Division, Lawrence Berkeley National Laboratory, California, USA
[3] Department of Chemical & Biomolecular Engineering, National Fuel Cell Research Center, University of California Irvine, California, USA
[4] Advanced Photon Source, Argonne National Laboratory, 9700 South Cass Avenue, Lemont, Illinois, USA
[5] Advanced Light Source, Lawrence Berkeley National Laboratory, California, USA
[6] Berkeley Institute for Data Science, University of California Berkeley, California, USA
[†] These authors contributed equally
*Corresponding authors: Iryna.zenyuk@uci.edu, dushizima@lbl.gov

Abstract
Inspection of Li-metal batteries during operation is essential to understanding how Li moves and why the battery degrades. *Operando* X-ray micro-computed tomography (µCT) provides an opportunity to observe the evolution of Li structures inside a Li-metal pouch cell. Segmentation is an essential step to quantitatively analyzing µCT datasets, but it is challenging to achieve on *operando* Li-metal battery datasets due to the low X-ray attenuation of the Li metal and the sheer size of the datasets. Herein, we report an iterative approach to training an Iterative Residual U-Net based network to segment *operando* X-ray µCT datasets of a solid-state Li metal pouch cell. Five Li-related components were extracted. With semantic segmentation, not only can we extract singular Li-related component changes, but we can also quantitatively analyze the diverse morphologies in the dataset. In our case, dead Li was visualized, and the volume and effective thickness of electrodes, deposited Li, and redeposited Li were calculated. We also discovered the spatial relationships between these components. The proposed approach is easily transferrable to other datasets and presents a unique method for analyzing battery performance. To the authors' knowledge, these Li dynamics have not been measured quantitatively using CT data before. This method brings new insight that can significantly benefit future Li-metal battery design.

Main
Li metal is a promising candidate as a battery anode material due to its high theoretical capacity (3,860 mAh g^{-1}) and high magnitude of thermodynamic potential (-3.06 V vs. SHE)[1]. In liquid electrolytes, Li metal is generally not stable, leading to various side reactions, the formation of solid electrolyte interphase (SEI), and dendrite formations[2]. Solid electrolytes can mitigate some of these issues, as they can form a more stable interface with Li metal[3,4]. Li-metal solid-state batteries (SSBs) have higher energy density compared to the current state-of-the-art Li-ion

batteries, resulting in lower battery weight and size. However, dendrite formation caused by inhomogeneous Li metal plating hinders the development of the SSBs. Most of the previous research on SSBs focused on dendrite structure or the growth of dendrites in small, nanoscale fields of view. A more in-depth understanding of the Li plating and stripping dynamics in SSBs in a larger field-of-view (micron-scale) is needed to overcome these challenges[1,5,6].

X-ray micro-computed tomography (μCT) has the spatial resolution necessary to capture dendrite formation[7]. *In situ/Operando* CT was used to detect the substructures formed on Li electrodes[8], to understand Li metal plating in symmetric Li/polymer electrolyte/Li batteries[4], to study the lithiation and Li plating in Li-graphite batteries with polymer electrolyte[6], and to reveal void formation caused by Li stripping at the interface between Li metal and solid-state electrolyte[9,10]. However, these studies imaged batteries with small active areas, leading to significant edge effects which cause streak artifacts or shading[11] as well as issues in electrochemical performance. Also, the batteries in some previous studies were constructed using a Swagelok cell. Swagelok cell are manufactured from a polyether ether ketone (PEEK) or other plastics to ensure X-rays are not too readily absorbed, and thus there is no guarantee that the cells are airtight. Our work reports on the development of a pouch cell designed for high-resolution synchrotron X-ray μCT imaging and demonstrates its feasibility. The coin-in-pouch cell design developed in this work enables high throughput imaging of batteries using operando X-ray CT while still achieving electrochemical performance comparable to other, smaller sized pouch cells.

A challenge in analyzing *operando* X-ray CT data is the sheer size of the datasets. One scan yielded tens of gigabytes of raw projection data, which was reconstructed into a multi-gigavoxel image stack. Here, we collected multiple image stacks, each containing over 26 billion voxels (stitched from three scans), so manual labeling all the data was not feasible. Furthermore, accurate segmentation of Li phase is an inherently complex problem. Li has a low atomic number and does not attenuate X-rays significantly, meaning that the contrast of Li structures in X-ray images is typically poor. Therefore, the pixel value difference between Li, voids, and other Li components is minimal. Traditional thresholding-based segmentation methods can be ineffective in such low-contrast settings due to noise and other imaging artifacts. However, machine learning, and in particular deep learning, can produce high-quality segmentations even with low-contrast and noisy images because they consider more complex, multi-resolution spatial components in addition to pixel intensity[36]. U-Net is a deep learning architecture initially developed for two-dimensional (2D) biomedical image segmentation but has become popular for many types of image segmentation, including CT images[12]. Like all such methods, it is trained on a small amount of labeled (i.e., pre-segmented) data, and once trained can produce segmentation predictions. Much effort [13-17] has been dedicated to exploiting machine learning to accelerate the analysis of CT data of batteries, most of which are focused on the electrodes, especially the cathodes.

In this paper, we performed *operando* X-ray μCT to track the Li dynamics of a solid-state Li-metal symmetric pouch cell during one cycle. With a monochromatic synchrotron beam, we collected 3D image volumes with high resolution (pixel size of 1.33 μm) of the same SSB at 25 different timesteps in one cycle. Using an Iterative Residual U-Net based segmentation algorithm, we processed all 25 volumes by splitting each volume into five classes: dendrite, pit, deposited li

(during charging), redeposited Li (during discharging), and background. We then analyzed the changes of each Li-related component and measured the spatial correlation between different components. Our main contribution is to provide an automated technique based on machine learning to segment large-scale *operando* µCT images and to perform quantitative analysis on morphological dataset of an energy device, foreseeing potential applications in quality control.

Operando X-ray CT

A Li/polymer electrolyte/Li symmetric pouch cell with an active area of 0.5 cm^2 was used in this study (Supplementary Fig. 1). Electrochemical impedance spectrum was collected at 25 °C before the cell was cycled (Supplementary Fig. 2). Full details about the cell assembly are presented in the Methods section.

Our *operando* X-ray CT study was conducted with the pouch cell mounted on the rotating stage by a clip (Fig. 1a) and connected to the potentiostat. The study was conducted for one full cycle (charge and discharge). A galvanostatic current of 1.5 mA cm^{-2} was periodically applied for 10 min and then interrupted with a ~20 minutes rest period in between (Fig. 1b). CT scans were collected during the rest periods, twenty-five scans in total over the entire experiment, to observe the evolution of the internal cell structure (Fig. 1c). By cycling the battery with this galvanostatic intermittent titration technique, the Li was able to dissolve and deposit during the rest periods and was less affected by the Li$^+$ concentration gradient at the interface. Therefore, the cycling curve can reveal voltage changes caused by the reaction rate difference on the electrode surface[18]. The envelope voltage constructed by connecting the maximum voltage of each current applied period (Supplementary Fig. 3) demonstrates this voltage change. The amplitude of the voltage peaking shape changed during the cycle. This means that the reaction rate effect on the voltage had been reduced, and Li accumulation occurred after the cycle[18-20].

Different components appeared at different stages during the full cycle (Fig. 1d). When checking the cross-section images, all five Li-related components could be recognized (note that all microCT figures are shown with inverted intensity scale, so lighter is less dense). At pristine state (before charging began), two Li metal electrodes were clearly shown, each of which had a thickness of ~100 µm. Between the Li metal electrodes, the polymer electrolyte was visible. For convenience and better presentation, we named the electrodes as the "Li-stripping side" and the "Li-plating side" based on their behavior during the charging stage. During charging, some new components appeared on the images, including deposited Li, dendrites, and pits. The deposited Li is the Li uniformly plated onto the electrode (Li-plating side). Dendrites are defined as the Li protruding out and having a height more than the uniformly plated Li (deposited Li). Pits are the components left after the Li was stripped non-uniformly on the electrode (Li-stripping side). During discharge, the pits were filled as deposited Li from the Li-plating side was redeposited on the Li-stripping side. This redeposited Li was added to the segmentation analysis. Some deposited Li and dendrites still appeared in some of the discharging images. The redeposited Li and pits only appeared on the Li-stripping side, while the deposited Li only existed on the Li-plating side. After one entire cycle, the dendrites remaining at the Li-plating side are considered dead Li. All analysis in this study was based on the above-mentioned Li-related components.

Machine learning-powered segmentation

The raw μCT scans were reconstructed (details are described in Methods) and yielded twenty-five grayscale image stacks. The overall pipeline to process the *operando* data consisted of image alignment and registration, region of interest (ROI) selection, image segmentation, and quantitative analysis (Fig. 2a). See Supplementary Note 1 for more details on these steps. To train an Iterative Residual U-Net for segmentation, labeled training data is required, but labeling vast, volumetric data is tedious. With μCT analysis of Li-metal battery morphology being a relatively new field, there do not exist publicly available labels or pre-trained models for segmentation tasks on similar datasets to our knowledge. Therefore, an iterative approach to training the network was developed.

Starting with a small number of 2D hand labels, an initial model was trained to segment pits, Li, and background, and the resulting predictions were used as starting points for further hand labeling. To make the labeling process more efficient, material phases like deposited Li, redeposited Li, and electrode were labeled individually. Thus, the segmentation was divided into several binary classification problems which were later combined with the results from the initial model to train the next, fully multi-class model. Fig. 2b shows the iterations in detail. Note that the initial labeling of pits and Li were made on the in-plane slices (see Supplementary Fig. 4 for illustrating demonstration), while later labels were made cross-sectionally. The in-plane slices near the electrodes have a higher density of the material phases of interest, making them more morphologically diverse than cross-section slices. Therefore, it is more efficient to train models from scratch with in-plane labels. However, distinguishing between some components, such as homogeneous electrode and electrolyte regions, is easier to classify in the cross-sectional views since they need context from the entire battery depth (see Supplementary Fig. 5 for demonstration). Finally, our cross-sectional model was refined using 42 hand-labeled cross-sectional slices across 11 of the 25 scans to improve classification accuracy in ambiguous regions. This final model achieved a testing accuracy of 98.8% and an overall intersection over union[12] (IoU) of 95.5% (Supplementary Table 1). More details about the model training are provided in the Methods and Supplementary Note 1.

After getting the semantic segmentation results, further post-processing was done, including choosing an appropriate ROI for quantitative analysis and refining the results by defining a reasonable spatial location for each component (see Supplementary Note 1 for more details). The *operando* CT imaging datasets for a cycling cell were segmented (Fig. 2c-d).

Quantitative analysis for Li-related components

After image segmentation, we performed a quantitative analysis of the Li-related components (Supplementary Fig. 6). More details about the analysis performed is included in Supplementary Note 2. The rendered volumes in Fig. 3a demonstrate the change of all components during the battery cycling at 1.5 mA cm^{-2}. As shown with the volume renderings, dendrites grew during charging and deposited Li appeared on the plating side while pits formed on the stripping side. When the applied current direction changed, the volume of the deposited Li on the plating side decreased while redeposited Li appeared to fill in the pits. Fig. 3b plots the volume changes of the dendrites (plating side), deposited Li (plating side during charging) and the redeposited Li

(stripping side during discharging). As expected, the volume of the dendrites increased and then decreased during the whole cycle. There were noticeably more dendrites at the beginning of the discharging than at the end of the charging. This indicates that Li was still moving during the rest period before discharging started. However, there were still some dendrites left after one full cycle, meaning that some Li with a volume of 1.11×10^7 μm³ had lost connection with the electrode and became "dead Li".

The change in thickness of both Li metal electrodes (excluding the contributions from deposited Li, dendrites or redeposited Li) are shown in Supplementary Fig. 7. The plating Li electrode grew during charging and shrank during discharging as expected, but its net thickness change was small. During charging, the stripping Li electrode shrank but did not increase during discharging. This could be due to the fact that the traveling Li did not integrate into the electrodes and only attached to the electrode surfaces as layers. If we include the deposited Li and redeposited Li into the thickness calculation, then the true Li evolution is revealed (Fig. 3c). During charging, the sum of thicknesses of components on the plating side (plating electrode and the deposited Li layer) increased from 107.7 μm to 140.1 μm. The increase slowed down after 60 min of charging (during the 7th charging segment) and almost stopped after 80 min (during the 9th charging segment). This is probably due to the newly plated Li integrating into the porous structure formed by the previously deposited Li. As with the ~1 μm resolution, sub micrometer porosity cannot be resolved with μCT. At the same time, the stripping side (stripping electrode and the redeposited Li) decreased from 112.9 μm to 101.7 μm with a rate of 0.93 μm /segment (10 min of charging). During discharging, the thickness of the stripping side increased at a rate of 2.47 μm /segment (10 min of discharging), and the final thickness of 130.5 μm was much higher than the pristine one of 112.9 μm. This was probably due to the nonuniform plating of the redeposited Li, which made the Li structure porous and loose. Also, the rate of decrease of the plating side thickness followed an exponential decay, meaning that the rate of thickness decrease dropped as discharge time increased. This could be due to the dead Li accumulation, which formed a tortuous Li$^+$ pathway and thus affected the Li$^+$ diffusion[18]. The deposited Li and redeposited Li are unlikely to be perfectly uniform even though we calculated their thickness with the assumption that their surfaces were flat.

The net Li volume in the ROI changed by 1.65×10^9 μm³ with a variation of 1.94×10^8 μm³ (Fig. 3d) during the cycle. The variation was probably due to error in the segmentation. This error could be caused by the porous structure of the Li. Fig. 3d also showed the traveling Li volume that is calculated from the cycling curve (see Supplementary Note 3 for more details). The amount of traveling Li calculated from the cycling curve (based on Faraday's Law) is larger than the one gained from the μCT data. If we converted the difference in amount of Li to the capacity, the missing capacity could be larger than 70% after one full cycle (Supplementary Fig. 8). It is possible that some of the applied current was used for interphase oxidation, which was observed in many of the batteries with solid-state electrolytes and is one of the primary causes of capacity fade in the SSBs[21-23]. Also, some nanostructures of Li may not be detected using μCT technique[24,25].

Li dynamics

The spatial evolution of Li dendrite and pits distributions over time were revealed by projecting the volumetric images onto a 2D, in-plane view (Fig. 4a-c, see Supplementary Note 2 for more details). The projected in-plane view projects all the dendrites or deposited Li present through-thickness of the battery onto a single projection. The area where no Li plated (dendrites or deposited) on the plating electrode decreased during charging, then increased during discharging, as expected. Almost all the deposited Li disappeared after one entire cycle (deposited Li occupation area decreased from 98.4% after charging to 0.16% after discharging), meaning that the deposited Li was still "conductive". However, dendrites occupied almost 30% of the ROI area at the half cycle and almost 12% when the cell finished one full cycle. This indicates that some of the Li on the dendrite structure were still conductive by maintaining connection to the electrode through Li nanostructures, while some Li dendrites were hard to "activate" and remained attached to the Li metal electrode. Also, the dendrite formed and grew at specific locations that did not change after the early stage of cycling. This indicates that the dendrite growth pattern was determined by the pristine structure of the cell rather than the later-formed components.

Pits at the stripping side were formed due to the nonuniform stripping. The colocalization was analyzed between the components on the plating side and the pits on the stripping side (Supplementary Fig. 9). However, no correlation was found between the 2D distribution of the pits and the dendrite or deposited Li. The pits formed in the charging stage and filled with redeposited Li in the discharging stage. By subtracting the flattened 3D data of the pits from the flattened 3D data of the redeposited Li, we learn about the filling status of the pits. Fig. 4d shows the 2D spatial distribution changes of pits. After one full cycle, almost the entire pit area was filled. This indicates that no defects prevented Li from redepositing on the stripping side. However, the filling was not compact since the thickness of the stripping side increased after a cycle. There might be voids between the redeposited Li and the electrode, meaning that the active area (where the redeposited Li was attached to the electrode) might not be the whole ROI area.

We can reveal more information by investigating the binary images of each Li components separately. Fig. 5a compares the location of the redeposited Li after a full cycle and the pits at a half cycle, which shows the map of voids between the redeposited Li and the stripping electrode. 53.9% of the ROI area was occupied by the voids, indicating that the contact area of the Li electrode and the solid electrolyte was 46.1%. The electrode position can be shown by the edge projection of the electrode (Fig. 5b and Supplementary Fig. 10). After charging, the gap between the plating electrode and stripping electrode increased ~39.3 μm. This demonstrates the battery swelling, which could be due to oxidation of the interphase or the void formation between the electrode and the deposited Li. No apparent changes in the electrode position were observed during the discharging.

Fig. 5c shows spatial relationship between the decrease of deposited Li and dendrites and the increase of the redeposited Li. Surprisingly, the spatial location where the deposited Li and dendrite volume decreased the most at the plating side was not correlated with the location where the redeposited Li increased the most at the stripping side. The Li-ion was not traveling in straight lines perpendicular to the electrodes but rather in a tortuous manner. This could be explained by

components or defects on the membrane (Supplementary Fig. 11), which could make the pathway of the traveling Li more complex.

Conclusion

Batteries need special care when being characterized since they cannot be exposed to air. Micro-CT is an ideal tool for understanding the internal structure of batteries since it can image with sufficient resolution to reveal Li component evolution while providing a large enough field of view for statistical analysis, all while the batteries are sufficiently sealed. With the help of deep learning, material phases can be segmented accurately and efficiently, even for very large volumetric datasets. We used an iterative training approach to achieve multi-class segmentation with satisfactory accuracy and minimal manual labeling. After segmenting the *operando* data into five different classes of dendrite, pits, deposited Li, redeposited Li and electrodes, the quantitative volume evolution of each component was revealed. Also, the Li traveling dynamics and its corresponding phenomena, like battery swelling, were detected by observing the electrode spatial changes.

We investigated the volume changes of different Li-related components. Some parts of the dendrites, which were defined as Li with abnormal height after plating on the electrode, struggle to maintain contact with the electrode. Thus, not all dendrites went back to the stripping side after one full cycle. Deposited Li plated uniformly on the electrode during charging and traveled back to the stripping side during discharge. However, after the Li redeposited to the stripping side, it was not fully attached to the electrode, leading to void formation between the redeposited Li and the electrode. These voids could potentially impede further redepositing of Li on the electrode during future cycling.

Our study demonstrated the possibility of quantifying the morphological evolution of the Li-related components within a sealed Li-metal battery. Furthermore, we provided an example of how to better analyze CT data for future experiments using a pipeline and the approach that can be transferred to other datasets.

Methods

Materials and Electrochemical Testing

Free-standing Li metal foil was used from FMC, with a thickness of ~100 μm. A polymer electrolyte membrane was provided as a research sample by Ionic Materials, Woburn, MA. The thickness of the polymer electrolyte was ~140 μm. The pouch cell was assembled in a configuration shown in Supplementary Fig. 1. A shim was used of 50 μm thickness to create a 0.8 cm diameter circle. Two polymer electrolyte membranes were punched in a circle having a diameter of 1.11 cm and placed on each side of the shim. Then two Li-metal electrodes were placed on the outside of each membrane. The metal tabs were connected to the Li-metal electrodes. The dimensions of the pouch cell were 1.5 cm x 3.75 cm. The cell was sealed with a vacuum sealer.

The cell was cycled at 1.5 mA cm^{-2} current density and 3.0 mAh cm^{-2}. The cell was mounted onto an X-ray CT rotating stage and was imaged in 10-minute intervals during the battery rest periods. No external pressure was applied to the cell.

Synchrotron X-ray CT Imaging

X-ray CT was carried out at Beamline 2-BM[33] at Advanced Photon Source (APS) at Argonne National Laboratory (ANL). The following optics were used: a 20 μm LuAG scintillator, 5x lenses and an sCMOS PCO Edge camera. The image resolution was 1.33 μm /pixel and the field-of-view was 3.4 mm. 27.5 keV energy was selected using a multilayer monochromator. Three Field of View (FOV) were recorded and stitched together to form a vertical height of > 3 mm. A 100 ms exposure time was used per projection, and 1500 projections were collected over 180 degrees of rotation. Tomographic reconstructions were performed using TomoPy[28-29] with the Gridrec algorithm [34-35]. Earlier works presented an in-depth description of algorithm parameters[30,31].

Image Processing and Segmentation

All data processing was done at the National Energy Research Scientific Computing Center (NERSC). Neural network training was performed on a single, 4-GPU Perlmutter node, using the distributed data parallel functionality in PyTorch. Since initial networks were trained using partial, imperfect labels made from scratch, we focused on qualitative improvement over quantitative segmentation metrics. For the early training, the data was split 85/15% into training and validation sets, respectively. Since our training data size varied significantly from network to network, we chose not to train for a fixed number of epochs. Instead, training was stopped after 1 hour or when validation accuracy did not improve for 10 iterations, whichever came first. However, our final set of labels consisting of of multi-class labels from 42 cross-sectional slices across 11 of the 25 scans was generated by refining previous predictions and was much more accurate. We split these final labels 72/13/15% into training, validation, and testing sets, respectively, which produced the final trained network and accuracy/IoU performance metrics. After segmentation, the processing and visualization were done in Fiji[32] and ORS Dragonfly Software (Version 2022.1).

Data Availability

XCT data, annotations and segmentation data will be available upon request as well as at Zenodo upon paper acceptance.

Code Availability

Python codes for microCT segmentation, batteryNET, were created by the authors and are described in this paper. These codes will be available upon paper acceptance and clearance with the LBNL Intellectual Property Office, following the DOE Advanced Scientific Computing Research (ASCR) recommendations.

Author contributions

Yang led data selection, microCT reconstruction and creation of diagrams for enhanced science understanding, together with Su and Perlmutter, who has also developed the machine learning algorithms for microCT. Ushizima and Quenum created the first codes for analysis of battery microCT within the team and they have lately participated in this algorithm validation and documentation. Shevchenko and Parkinson were the beamline scientists responsible for sample imaging. Yang and Zenyuk performed battery tests associated to the pouch cell charge/discharge. Ushizima and Zenyuk formulated the project, and led the research activity planning, execution, and coordination. All authors have contributed to the writing.

Competing Interests

The Authors declare no Competing Financial or Non-Financial Interests.

Reference

1   Hatzell, K. B. *et al.* Challenges in Lithium Metal Anodes for Solid-State Batteries. *ACS Energy Letters* **5**, 922-934, doi:10.1021/acsenergylett.9b02668 (2020).
2   Yu, Y., Liu, Y. & Xie, J. Building Better Li Metal Anodes in Liquid Electrolyte: Challenges and Progress. *ACS Applied Materials & Interfaces* **13**, 18-33, doi:10.1021/acsami.0c17302 (2021).
3   Shen, Y. *et al.* Unlocking the Energy Capabilities of Lithium Metal Electrode with Solid-State Electrolytes. *Joule* **2**, 1674-1689, doi:https://doi.org/10.1016/j.joule.2018.06.021 (2018).

4   Lepage, W. S. *et al.* Lithium Mechanics: Roles of Strain Rate and Temperature and Implications for Lithium Metal Batteries. *Journal of The Electrochemical Society* **166**, A89-A97, doi:10.1149/2.0221902jes (2019).

5   Krauskopf, T., Richter, F. H., Zeier, W. G. & Janek, J. Physicochemical Concepts of the Lithium Metal Anode in Solid-State Batteries. *Chemical Reviews* **120**, 7745-7794, doi:10.1021/acs.chemrev.0c00431 (2020).

6   Albertus, P. *et al.* Challenges for and Pathways toward Li-Metal-Based All-Solid-State Batteries. *ACS Energy Letters* **6**, 1399-1404, doi:10.1021/acsenergylett.1c00445 (2021).

7   Varipore™: A Powerful Manufacturing Platform for Fuel Cell and Electrolyzer Applications. *ECS Meeting Abstracts*, doi:10.1149/ma2019-02/37/1734 (2019).

8   Harry, K. J., Hallinan, D. T., Parkinson, D. Y., MacDowell, A. A. & Balsara, N. P. Detection of subsurface structures underneath dendrites formed on cycled lithium metal electrodes. *Nature Materials* **13**, 69-73, doi:10.1038/nmat3793 (2014).

9   Tippens, J. *et al.* Visualizing Chemomechanical Degradation of a Solid-State Battery Electrolyte. *ACS Energy Letters* **4**, 1475-1483, doi:10.1021/acsenergylett.9b00816 (2019).

10   Lewis, J. A. *et al.* Linking void and interphase evolution to electrochemistry in solid-state batteries using operando X-ray tomography. *Nature Materials* **20**, 503-510, doi:10.1038/s41563-020-00903-2 (2021).

11   Joseph, P. M. & Spital, R. D. The exponential edge-gradient effect in X-ray computed tomography. *Physics in Medicine and Biology* **26**, 473-487, doi:10.1088/0031-9155/26/3/010 (1981).

12   Ronneberger, O., Fischer, P. & Brox, T. U-Net: Convolutional Networks for Biomedical Image Segmentation. *International Conference on Medical image computing and computer-assisted intervention.* 234-241 (Springer).

13   Ho, A. S. *et al.* 3D Detection of Lithiation and Lithium Plating in Graphite Anodes during Fast Charging. *ACS nano* (2021).

14   Allen, E. *et al.* Spatial Quantification of Microstructural Degradation during Fast Charge in 18650 Lithium-Ion Batteries through Operando X-ray Microtomography and Euclidean Distance Mapping. *ACS Applied Energy Materials*, doi:10.1021/acsaem.2c02397 (2022).

15   Li, J. *et al.* Dynamics of particle network in composite battery cathodes. *Science* **376**, 517-521, doi:10.1126/science.abm8962 (2022).

16   Zhang, K., Nguyen, T.-T., Su, Z. & Demortière, A. Self-supervised image quality assessment for X-ray tomographic images of Li-ion battery. *npj Computational Materials* **8**, 194, doi:10.1038/s41524-022-00870-z (2022).

17   Su, Z. *et al.* Artificial neural network approach for multiphase segmentation of battery electrode nano-CT images. *npj Computational Materials* **8**, 30, doi:10.1038/s41524-022-00709-7 (2022).

18   Chen, K.-H. *et al.* Dead lithium: mass transport effects on voltage, capacity, and failure of lithium metal anodes. *Journal of Materials Chemistry A* **5**, 11671-11681, doi:10.1039/C7TA00371D (2017).

19   Wood, K. N. *et al.* Dendrites and Pits: Untangling the Complex Behavior of Lithium Metal Anodes through Operando Video Microscopy. *ACS Central Science* **2**, 790-801, doi:10.1021/acscentsci.6b00260 (2016).

20   Shi, P. *et al.* Electrochemical Diagram of an Ultrathin Lithium Metal Anode in Pouch Cells. *Advanced Materials* **31**, 1902785, doi:https://doi.org/10.1002/adma.201902785 (2019).

21   Wang, S., Xu, H., Li, W., Dolocan, A. & Manthiram, A. Interfacial Chemistry in Solid-State Batteries: Formation of Interphase and Its Consequences. *Journal of the American Chemical Society* **140**, 250-257, doi:10.1021/jacs.7b09531 (2018).

22   Schwietert, T. K. *et al.* Clarifying the relationship between redox activity and electrochemical stability in solid electrolytes. *Nature Materials* **19**, 428-435, doi:10.1038/s41563-019-0576-0 (2020).

23   Cheng, E. J., Kushida, Y., Abe, T. & Kanamura, K. Degradation Mechanism of All-Solid-State Li-Metal Batteries Studied by Electrochemical Impedance Spectroscopy. *ACS Applied Materials & Interfaces* **14**, 40881-40889, doi:10.1021/acsami.2c09841 (2022).

24   Luo, S. *et al.* Nanostructure of the Interphase Layer between a Single Li Dendrite and Sulfide Electrolyte in All-Solid-State Li Batteries. *ACS Energy Letters* **7**, 3064-3071, doi:10.1021/acsenergylett.2c01543 (2022).

25   Ho, A. S. *et al.* Uncovering the Relationship between Diameter and Height of Electrodeposited Lithium Protrusions in a Rigid Electrolyte. *ACS Applied Energy Materials* **3**, 9645-9655 (2020).

26   De Andrade, V. *et al.* Nanoscale 3D imaging at the advanced photon source. *SPIE Newsroom* **10**, 006461 (2016).

27   De Carlo, F. *et al.* Scientific data exchange: a schema for HDF5-based storage of raw and analyzed data. *Journal of synchrotron radiation* **21**, 1224-1230 (2014).

28   Gürsoy, D. A., De Carlo, F., Xiao, X. & Jacobsen, C. TomoPy: a framework for the analysis of synchrotron tomographic data. *Journal of Synchrotron Radiation* **21**, 1188-1193, doi:10.1107/s1600577514013939 (2014).

29   Pelt, D. M. *et al.* Integration of TomoPy and the ASTRA toolbox for advanced processing and reconstruction of tomographic synchrotron data. *Journal of Synchrotron Radiation* **23**, 842-849, doi:10.1107/s1600577516005658 (2016).

30   Serov, A. *et al.* Nano-structured platinum group metal-free catalysts and their integration in fuel cell electrode architectures. *Applied Catalysis B: Environmental* **237**, 1139-1147, doi:10.1016/j.apcatb.2017.08.067 (2018).

31   Shum, A. D. *et al.* Investigating Phase-Change-Induced Flow in Gas Diffusion Layers in Fuel Cells with X-ray Computed Tomography. *Electrochimica Acta* **256**, 279-290, doi:10.1016/j.electacta.2017.10.012 (2017).

32   Schindelin, J. *et al.* Fiji: an open-source platform for biological-image analysis. *Nature Methods* **9**, 676-682, doi:10.1038/nmeth.2019 (2012).

33   Nikitin, V., Tekawade, A., Duchkov, A., Shevchenko, P. & De Carlo, F. Jour. Synchrotron Rad. 29, 816-828 (2022).

34   Dowd, B. A., Campbell, G. H., Marr, R. B., Nagarkar, V., Tipnis, S., Axe, L., & Siddons, D. P. (1999). Developments in synchrotron X-Ray Computed Microtomography at the National Synchrotron Light Source. *Proceedings of SPIE - The International Society for Optical Engineering*, *3772*, 224-236.

35   Rivers, Mark L. "tomoRecon: High-speed tomography reconstruction on workstations using multi-threading." In Proc. SPIE, volume 8506, 85060U–85060U–13 (2012).

36   Chauhan, N. K. & Singh, K. in 2018 International conference on computing, power and communication technologies (GUCON). 347-352 (IEEE).

Figures

Machine Learning Powered Observation of Lithium Plating Dynamics in a Solid-State Battery with *Operando* X-ray Computed Tomography

Ying Huang[1†], David Perlmutter[2†], Andrea Fei-Huei Su[3], Jerome Quenum[2], Pavel Shevchenko[4], Dilworth Parkinson[5], Iryna V. Zenyuk[3*], Daniela Ushizima[2*]

[1] Department of Materials Science & Engineering, National Fuel Cell Research Center, University of California Irvine, California, USA
[2] Computational Research Division, Lawrence Berkeley National Laboratory, California, USA
[3] Department of Chemical & Biomolecular Engineering, National Fuel Cell Research Center, University of California Irvine, California, USA
[4] Advanced Photon Source, Argonne National Laboratory, 9700 South Cass Avenue, Lemont, Illinois, USA
[5] Advanced Light Source, Lawrence Berkeley National Laboratory, California, USA
[†] These authors contributed equally
*Corresponding authors: Iryna.zenyuk@uci.edu, dushizima@lbl.gov

Fig. 1 *Operando* X-ray imaging of the pouch cell during cycling

a. Schematic of *operando* setup for CT imaging experiments of a cycling pouch cell.

b. Representative 3D datasets collected showing the evolution of the internal pouch cell during one full charge and discharge cycle.

c. Cycling curve measured during the *operando* CT experiment at 1.5 mA cm^{-2}. Scans were taken during pouch cell charge/discharge rest periods.

d. Representative grayscale image showing the Li-related components to be segmented.
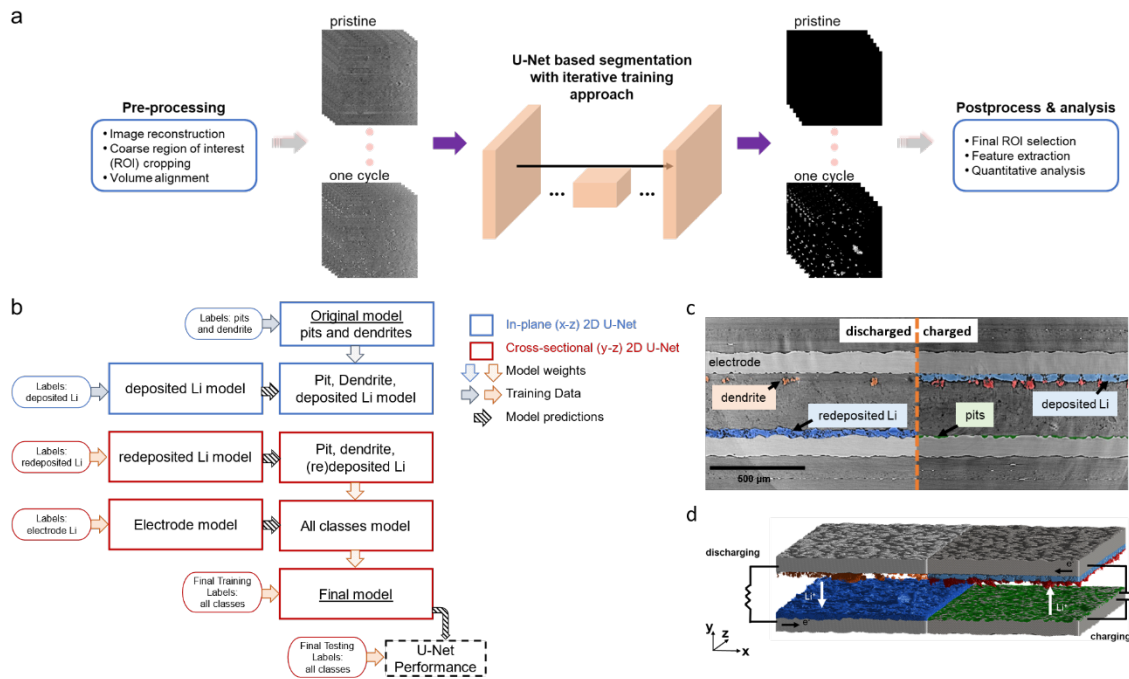
Fig. 2 Pipeline of the *operando* imaging data processing.

a. Image processing pipeline from raw data to quantitative results

b. Detailed schematic representation of iterative U-Net model training

c, d. Illustration of the segmentation results of the pouch cell after half and full cycle: **c**, representative 2D cross-section image and **d**, 3D structure. The arrows indicate how Li-ions and electrons moved during the charging and discharging stages.
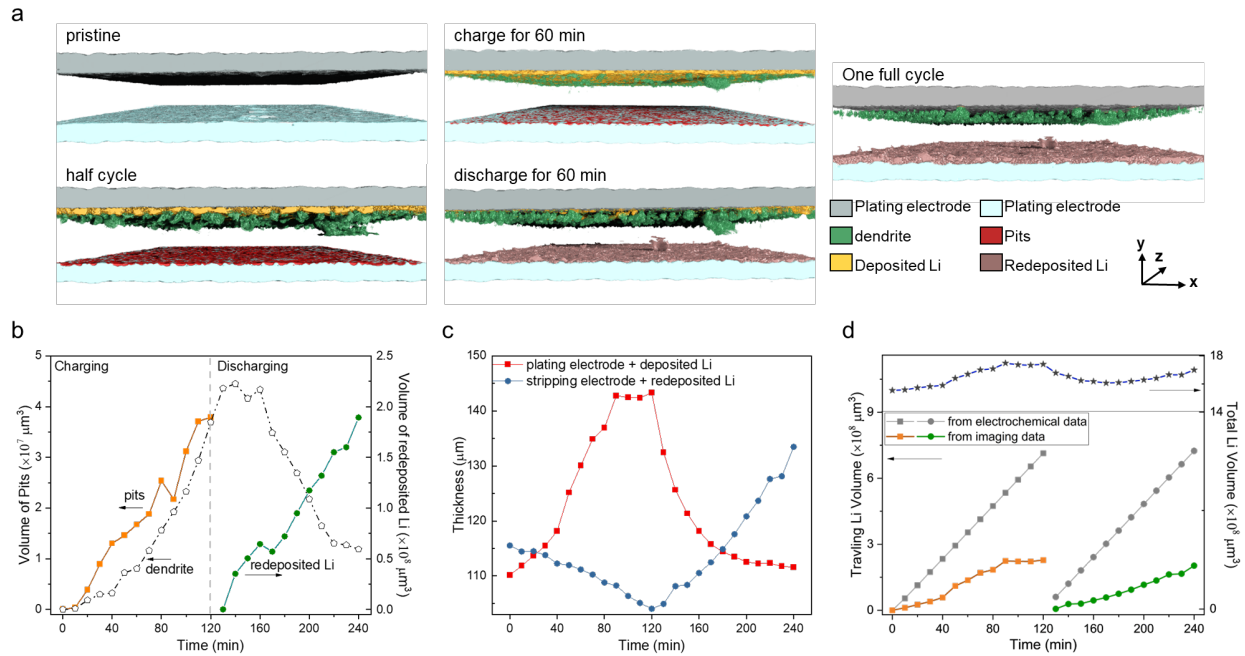
Fig. 3 Quantitative analysis of Li-related components.

a. 3D rendering of the segmented data at selected time steps. Each Li phase is rendered in a different color.

b. Volume change of dendrites, deposited Li, and redeposited Li over the full cycle, as extracted from the segmentations. The x-axis includes times when current is being applied only, not resting periods.

c. Effective electrode thickness on the plating side (excluding dendrites) and stripping side over time. The x-axis includes times when current is being applied only, not resting periods.

d. Transformation of traveling Li calculated from μCT data and the cycling curve. The total Li volume is calculated from the μCT data. The x-axis includes times when current is being applied only, not resting periods.
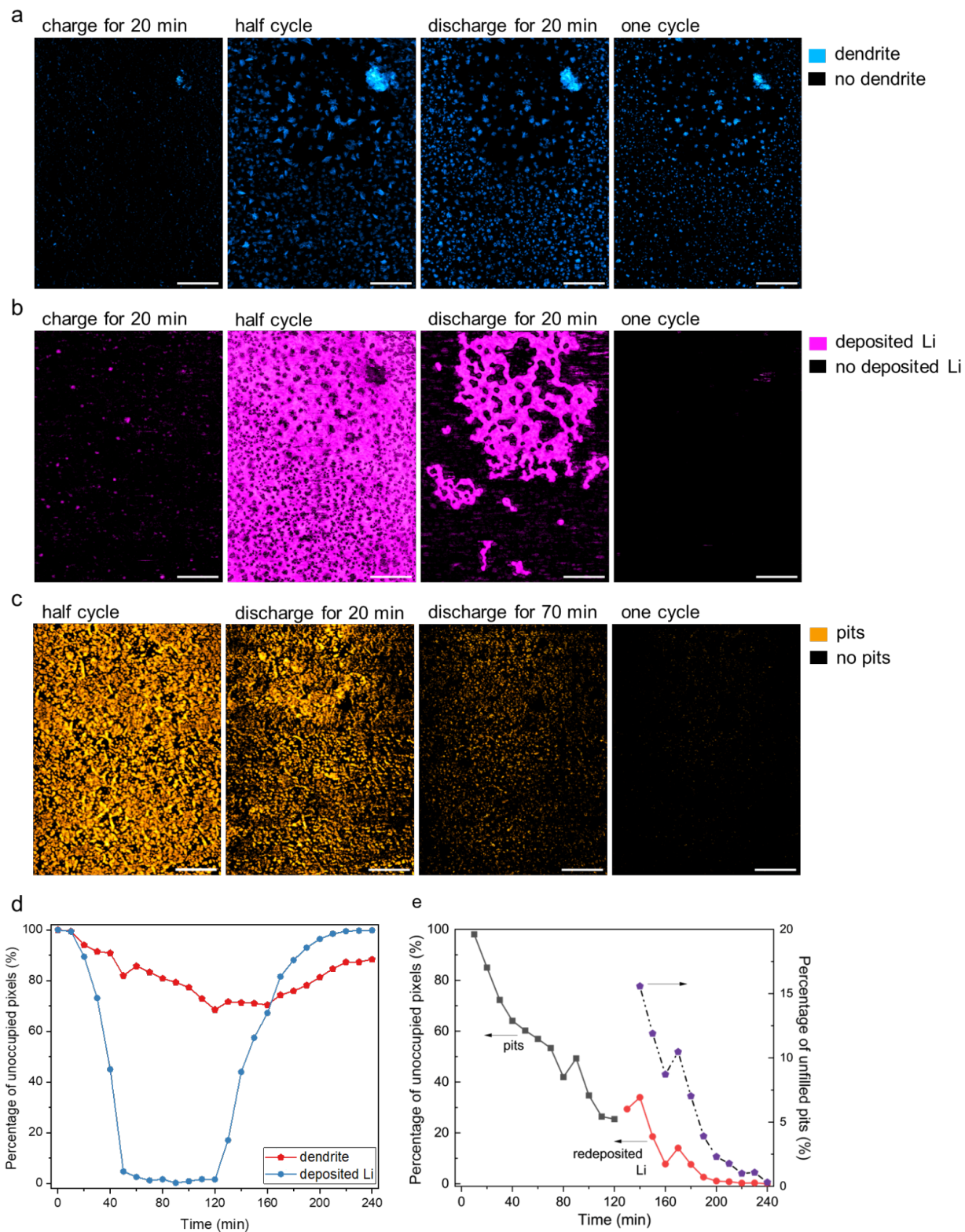
Fig. 4 Two-dimensional (2D) Distribution of the Li-related components.

a. Evolution of the dendrite spatial distribution in 2D in-plane views (flattened 3D data). Dendrites are plotted in cyan. Scale bar: 500 μm.

b. Evolution of deposited Li spatial distribution in 2D in-plane views (flattened 3D data). Deposited Li is plotted in magenta. Scale bar: 500 μm.

c. Evolution of the unfilled pit spatial distribution during discharging in 2D in-plane views (flattened 3D data). The half-cycle figure (left) shows the pits formed during the charging stage. The orange color shows the area where the pits were not fully filled. Scale bar: 500 μm.

d. Proportion of 2D in-plane view pixels not occupied by dendrite (blue) and deposited Li (red) over the full cycle. The x-axis includes times when current is being applied only, not resting periods.

e. Proportion of 2D in-plane view pixels not occupied by pits (black) and redeposited Li (red) over the full cycle. Purple shows the percentage of pits remaining unfilled during discharge. The x-axis includes times when current is being applied only, not resting periods.
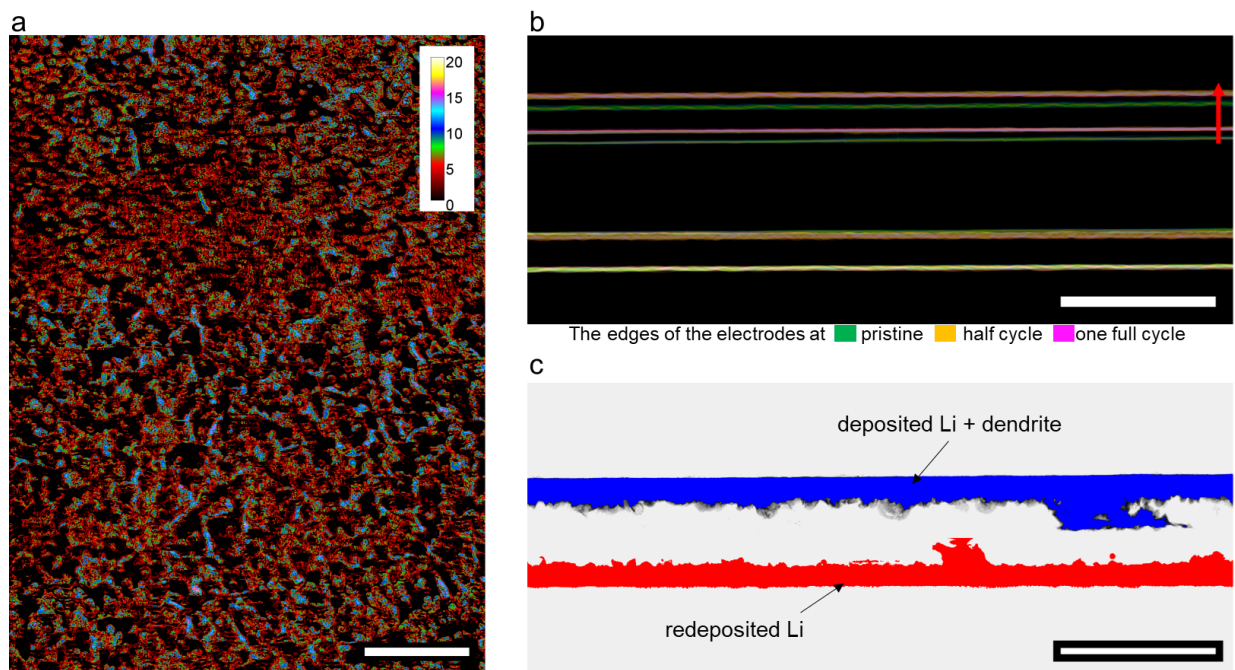
Fig. 5 Comparison between Li-components at pristine, half cycle, and one full cycle.

a. Map of voids between redeposited Li and Li-stripping side electrode after the full cycle. The voids are defined as the pits (formed during charging) that were not occupied by redeposited Li after discharging. Scale bar: 500 μm. Color bar represents the depth of the voids, unit: μm.

b. Displacement of electrode over full cycle. The green, orange, and magenta colors represent the edges of the pristine electrodes, after a half cycle, and after the full cycle, respectively (note: the lowest electrode didn't move significantly during the cycle, so all 3 colors overlap and appear yellow). Scale bar: 500 μm.

c. Map of traveling Li- components evolution during discharging (from half to full cycle), in cross-sectional view (flattened 3D data). Blue shows where deposited Li and dendrites decreased and red shows where redeposited Li increased. Scale bar: 500 μm.

Detecting Lithium Plating Dynamics in a Solid-State Battery with *Operando* X-ray Computed Tomography using Machine Learning

Ying Huang[1†], David Perlmutter[2†], Andrea Fei-Huei Su[3], Jerome Quenum[2], Pavel Shevchenko[4], Dilworth Parkinson[5], Iryna V. Zenyuk[3*], Daniela Ushizima[2,6*]

[1] Department of Materials Science & Engineering, National Fuel Cell Research Center, University of California Irvine, California, USA
[2] Computational Research Division, Lawrence Berkeley National Laboratory, California, USA
[3] Department of Chemical & Biomolecular Engineering, National Fuel Cell Research Center, University of California Irvine, California, USA
[4] Advanced Photon Source, Argonne National Laboratory, 9700 South Cass Avenue, Lemont, Illinois, USA
[5] Advanced Light Source, Lawrence Berkeley National Laboratory, California, USA
[6] Berkeley Institute for Data Science, University of California Berkeley, California, USA
[†] These authors contributed equally
*Corresponding authors: Iryna.zenyuk@uci.edu, dushizima@lbl.gov

Table of Contents:

Supplementary Note 1: Image pre-processing and segmentation

Registration

The raw μCT reconstructions from all 25 scans were registered before labeling and segmentation. First, we roughly aligned the electrodes to be perpendicular in-plane (x-z plane in Fig. 1b) by applying fixed rotations to each cross-sectional slice, first in x-y and then y-z. The angles were chosen by eye from visualized slices in a Jupyter notebook. Next, we fixed the geometry of the final (240 min) scan, cropped the volume to an initial ROI (of 3896×1707×698 voxels), and precisely registered and cropped the remaining scans to the fixed volume using the ITK registration toolbox[1]. Each registration iteratively optimized a 6 parameter, 3D rigid-body transformation (3 rotations and 3 translations) with sub-voxel resolution to maximize the voxel-wise cross-correlation. Registration of the entire ROI was too computationally demanding, so we used a 300×300×300 voxel sub-volume centered on material defects known to be static across the experiment. Also, since some gross, non-rigid deformation was present in the battery throughout the experiment, we averaged the registrations from several sub-volumes distributed across the battery to ensure we achieved a reasonable fit everywhere.

Neural Network Segmentation

Convolutional neural networks (CNNs) treat image segmentation as pixel-wise classification into distinct, pre-defined classes and are known to give state of the art segmentation performance. Since our data volumes are very large (3896×1707 pixels per slice), we subdivided each slice into fixed-size patches which before inputting to the neural network. Models were trained in PyTorch, using standard cross-entropy loss and the Adam optimizer. For inference, we also use patches but with 25% overlap to mitigate the loss of classification accuracy near the patch edges[3,4] The multiple predictions from overlapped regions were averaged before applying the softmax function. Supplementary Fig. S12 shows sample outputs of the model considered in this work.

The U-Net architecture was first introduced in 2015 by Ronneberger et al.[2] for the semantic segmentation of biomedical images. We refer interested readers to the referred paper for details about the architecture of the network. In our work, we used the U-Net implementation in MONAI[5], which is based on a Residual U-Net architecture[6]. Residual U-Net improves upon the original U-Net by adding residual connections between input and output blocks within the same level (i.e. resolution) in both the encoder and decoder[7]. The networks consisted of seven levels, with each level containing two blocks, and each block consisting of, in order, convolutional, parametric ReLU, dropout (20%), and batch normalization layers. Adjacent levels were connected with max pool 2x2 downsampling layers in the encoder, and strided transpose convolutional 2x2 upsampling layers in the encoder. As in standard U-Net, skip connections connected equivalent encoder and decoder levels. We used 512 pix × 512 pix inputs, a 3x3 convolutional kernel, and 32, 64, 128, 256, 512, 512, 512 channels for each of the seven levels, respectively.

Post-processing

Some post-processing was done on the raw segmentation results before analysis. First, we chose to remove the edges of the full volumes, where image quality was poorer and inconsistent segmentation results were given. Our final analysis ROI was 2280×1707×698 voxels. Next, we split the electrode and deposited Li class into two subclasses each based on depth. The ROI was divided into two sub-volumes, each 2280×1707×349 voxels. The voxels closer to the stripping Li were relabeled redeposited Li, while the pixels closer to the plating Li remained deposited Li. A similar operation was done to get the volumes of the striping Li electrode and the plating Li electrode.

Supplementary Note 2: Quantitative analysis and image manipulation

1. Quantitative analysis

The quantitative analysis was conducted based on the segmentation results and voxel size of the µCT. The equations were shown as follows.

$$Feature\ Volume =\ Labeled\ Voxel\ \times (1.33\ \mu m)^3$$

$$Feature\ Thickness = \frac{Labeled\ Voxel\ \times (1.33\ \mu m)^3}{ROI\ area}$$

Notice that in our case,

$$ROI\ area =\ 1707\ \times 2280\ \times (1.33\ \mu m)^2$$

2. Flatten 3D

Flattening the 3D image stack can make visualization and analysis simpler. In this study, we used Z-project in Fiji Image J[8] on the binary image stacks representing individual segmented classes. We applied Z-project by either summing or averaging the pixel values along the y-axis (perpendicular to the electrode plane). A sum Z-project calculates the total thickness of the class at a given location, while averaging gives the density.

3. Colocalization

The colocalization analysis in this study was done using Coloc 2[9], which is a plugin of Fiji Image J[8]. Coloc shows the correlation between the 2D spatial map of different segmented classes. The Pearson's correlation coefficient summarized the strength of this correlation; a correlation coefficient of 1 means perfect correlation, 0 means no correlation, and -1 means perfect anti-correlation.

Supplementary Note 3: Traveling Li volume from the electrochemical curve

In this study, the galvanostatic current was periodically applied twenty-four times over one cycle, for 10 min each. Thus, all the calculations were done based on one current-applied period (10 min).

The capacity (unit: mAh) of the battery gained from one current-applied period is:

$$Capacity_{10min} = I_{applied} \times 10\ min \times \frac{1\ h}{60\ min}$$

The specific capacity of Li-metal is 3860 mAh g^{-1}. Thus, the mass of the Li traveled in one current-applied period can be calculated as:

$$Mass_{10min} = \frac{Capacity_{10min}}{3860\ mAh/g}$$

With the information that the density of Li metal is 0.534 g cm^{-3}, the volume of the Li traveled in one current-applied period can be gained by:

$$Volume_{10min} = \frac{Mass_{10min}}{0.534\ g/cm^3}$$

Supplementary Figures and Tables

Supplementary Fig. 1 The schematic of the assembled pouch cell for *operando* CT experiment

Supplementary Fig. 2 EIS data of the pristine assemble pouch cell

Supplementary Fig. 3 Voltage profile of galvanostatic intermittent titration cycling for one cycle

Supplementary Fig. 4 Example of the labels in in-plane view

Supplementary Fig. 5 Example of a small batch of labels in cross-sectional view

Supplementary Fig.6 Quantitative analysis based on the segmentation results from final U-Net model

Supplementary Fig.7 Changes of the effective thickness of the electrodes during one cycle

Supplementary Fig. 8 Capacity calculated from CT imaging data over the capacity calculated from cycling curve

Supplementary Fig. 9 Person's correlation coefficient between the 2D distribution of Pits and deposited Li or dendrite

Supplementary Fig. 10 Flattened 3D data (average) of the edge of the segmented electrodes at pristine, half cycle and full cycle

Supplementary Fig. 11 Representative thru-plane images of the solid-state electrolyte region

Supplementary Fig. 12 Examples of the final prediction of the U-Net model

Supplementary Table 1 Breakdown of per-class test set IoU for final cross-sectional U-Net model

a

3.75 cm

1.50 cm

b

red shim
t=50 µm

Li
t=100 µm

polymer electrolyte
t=100 µm
d=1.11 cm

Active area
d=0.80 cm
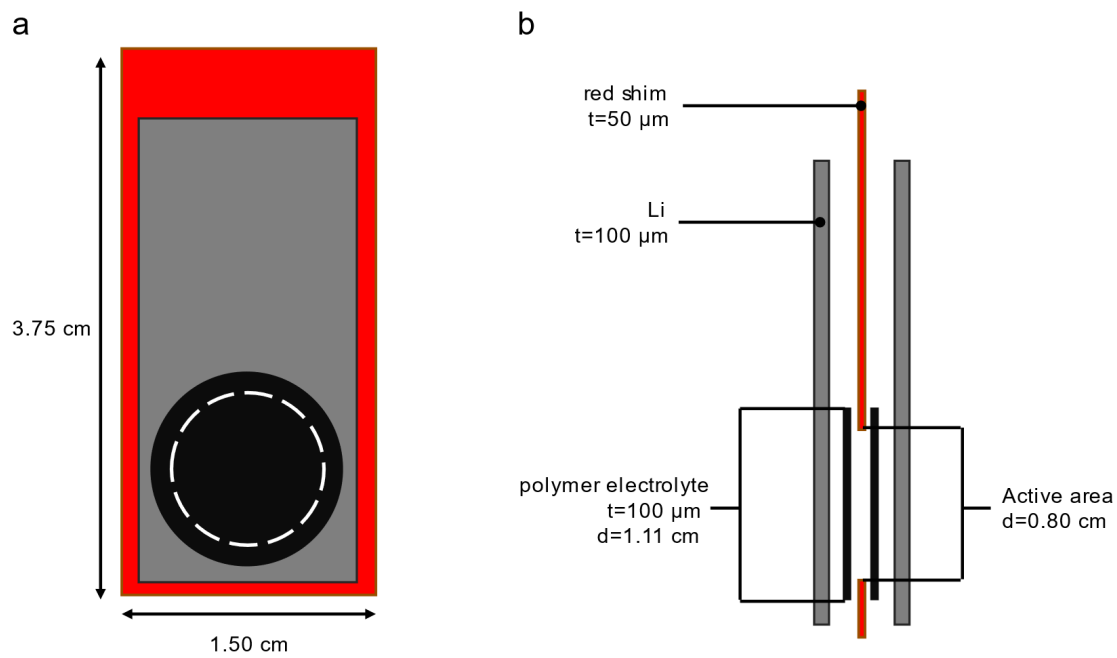
Supplementary Fig. 1 Schematic of the assembled pouch cell for *operando* CT experiment
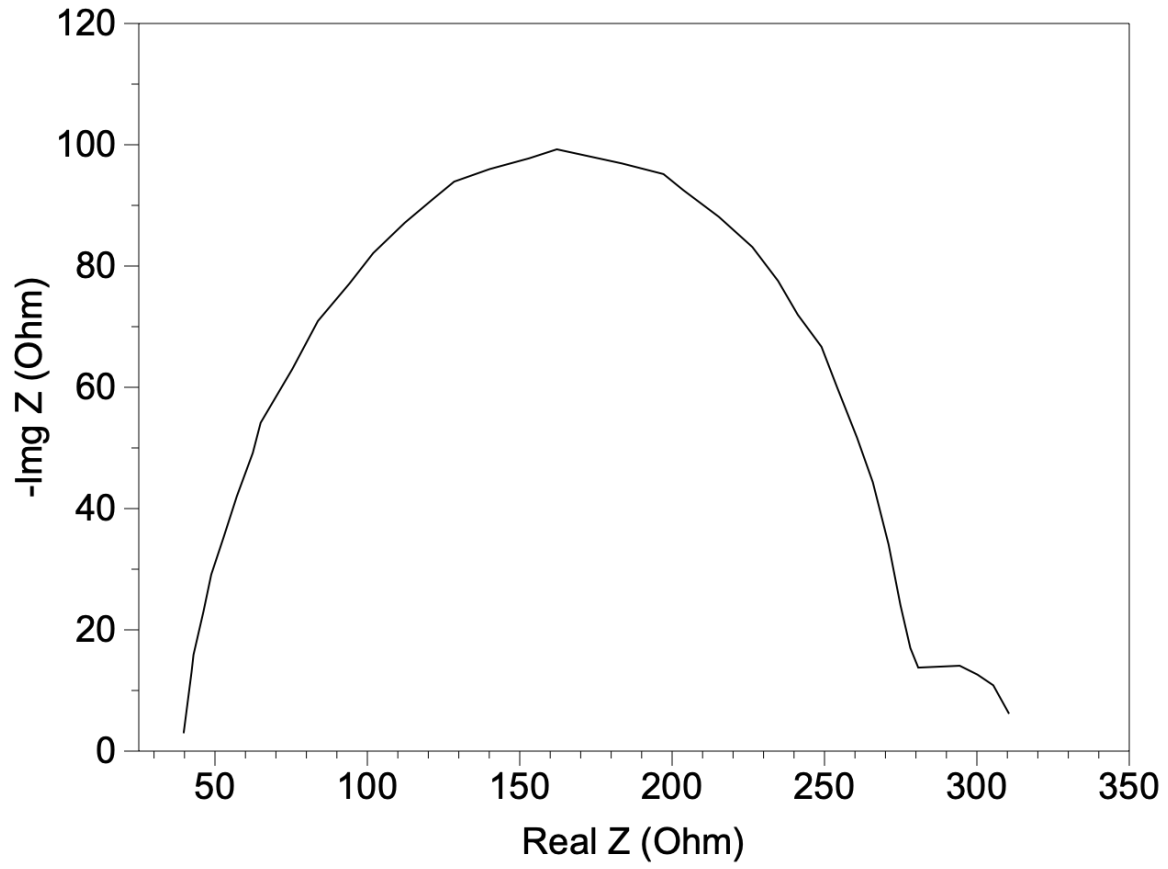
**Supplementary Fig. 2** EIS data of the pristine assembled pouch cell
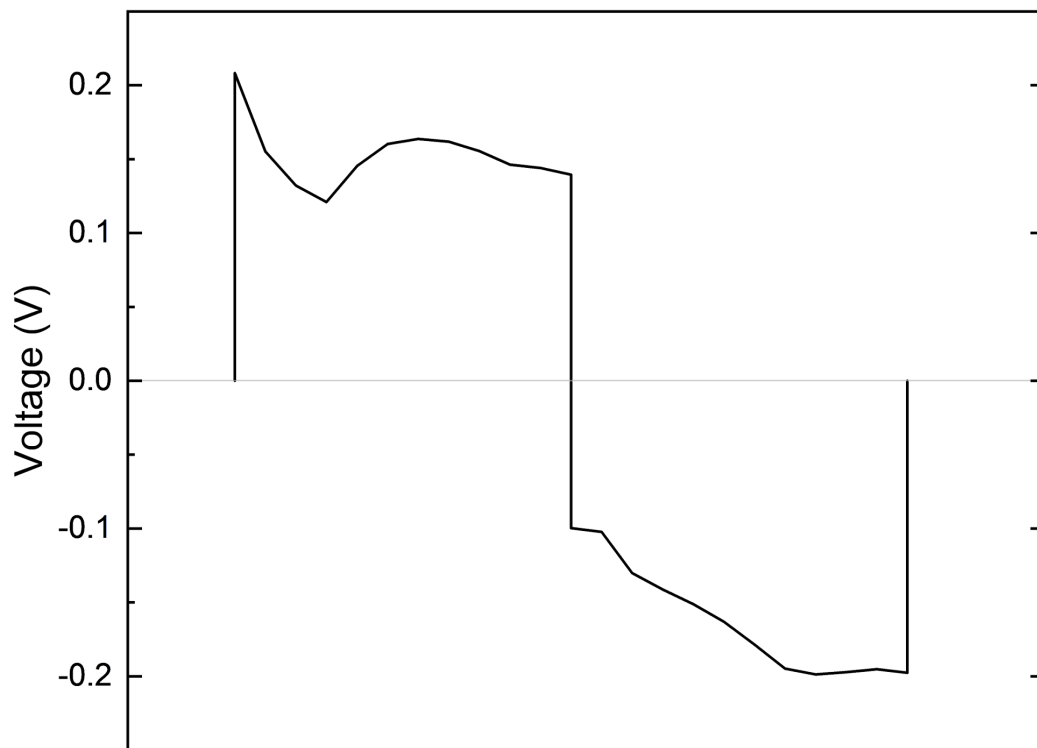
Supplementary Fig. 3 Voltage profile of galvanostatic intermittent titration cycling over one cycle. The profile is constructed by connecting the maximum voltage at each transient period.
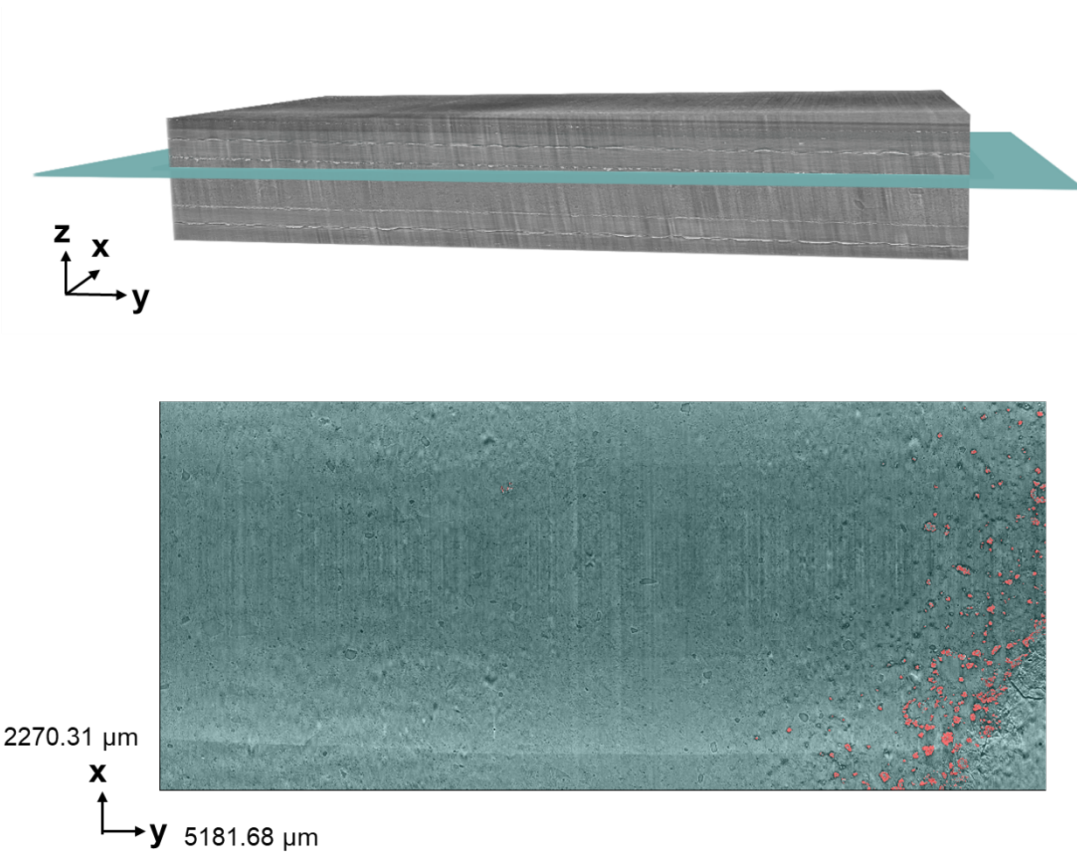
Supplementary Fig. 4 Example of an in-plane view hand label. Red represents dendrite and blue represents background.

928.34 μm

z

x 2270.31 μm
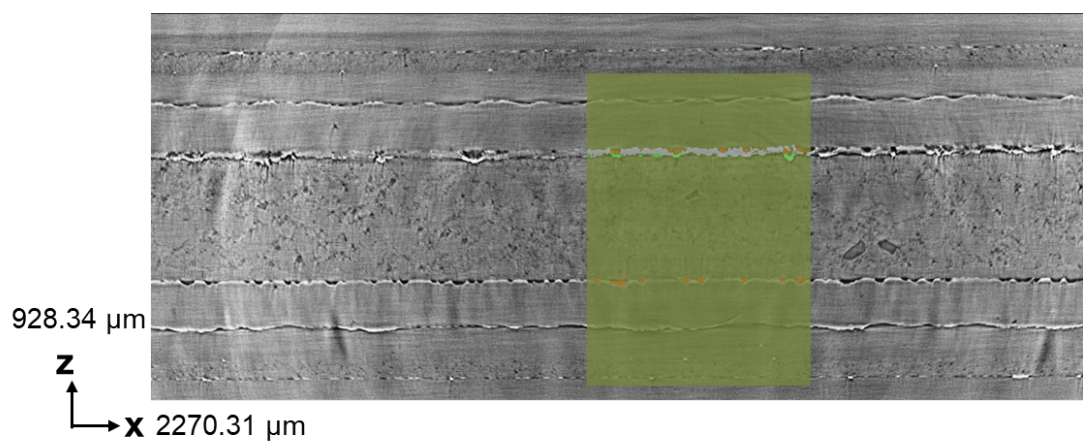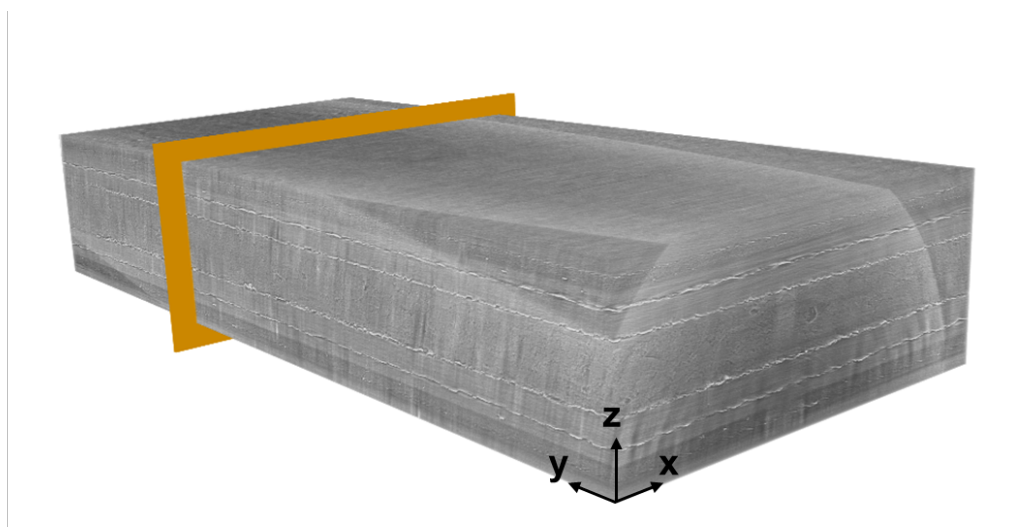
Supplementary Fig. 5 Example of a partial cross-sectional labels. The colored overlay shows the labels painted on top of a the grayscale image. Yellow pixels, representing background, make up the largest labeled section. Green, red, orange and grey pixels represent dendrite, deposited Li, pit and electrode pixels, respectively. However, most of the image is unlabeled, and so appears as simply a grayscale image.
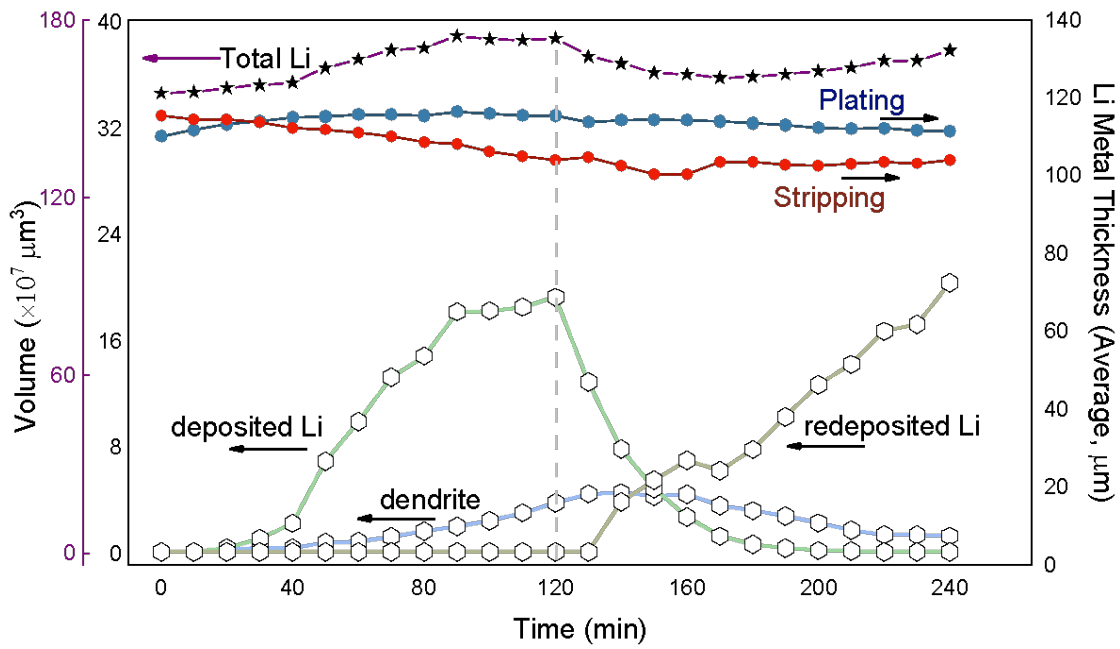
Supplementary Fig.6 Quantitative analysis of material phase evolution based on segmentation results from final U-Net model. The x-axis includes times when current is being applied only, not resting periods.
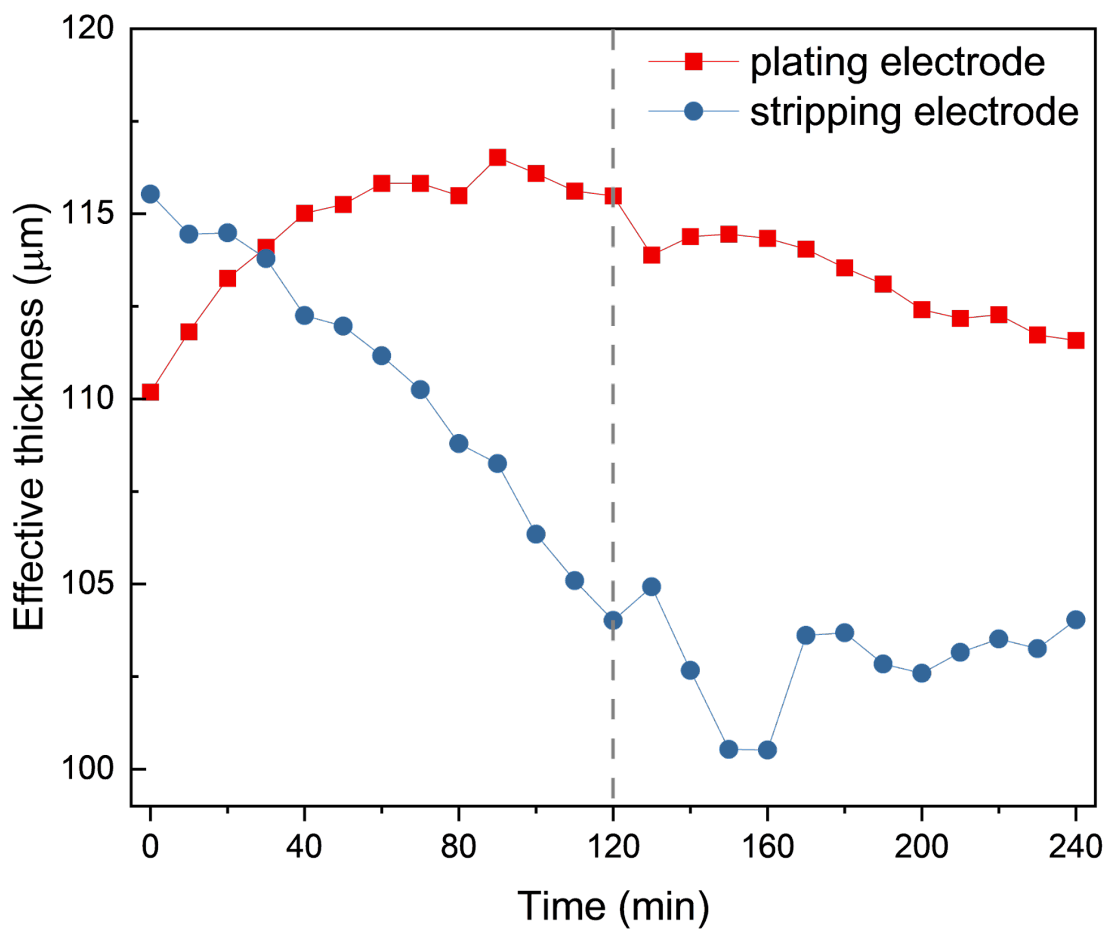
Supplementary Fig.7 Change in the effective thickness of the electrodes during one cycle. The x-axis includes times when current is being applied only, not resting periods.
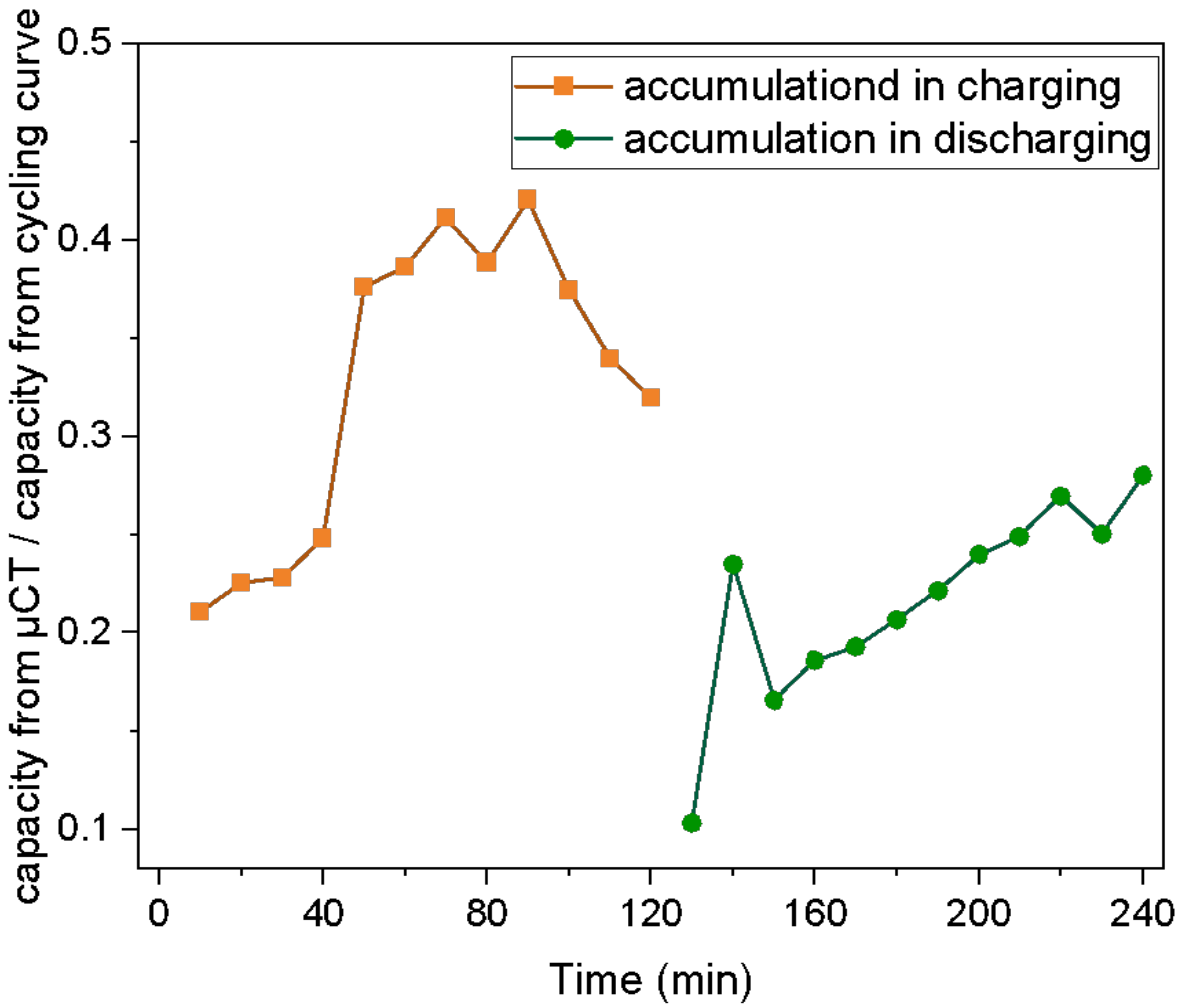
Supplementary Fig. 8 Capacity calculated from CT imaging data divided by the capacity calculated from cycling curve. The accumulated capacity from the CT data in the charging stage was calculated from Li-features voxels in the plating side minus the original plating electrode voxels. The discharging stage was calculated from Li-features voxels in the stripping side minus the original stripping electrode voxels. The x-axis includes times when current is being applied only, not resting periods.
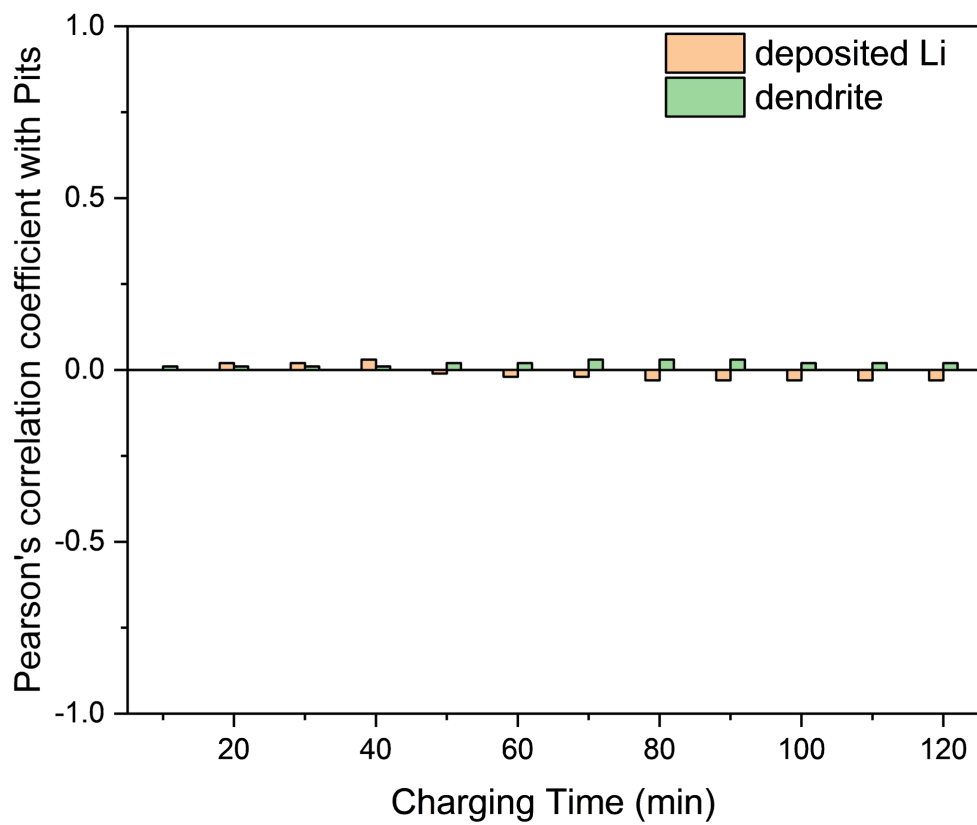
Supplementary Fig. 9 Person's correlation coefficient between the 2D distribution of Pits and deposited Li or dendrite. The x-axis includes times when current is being applied only, not resting periods.
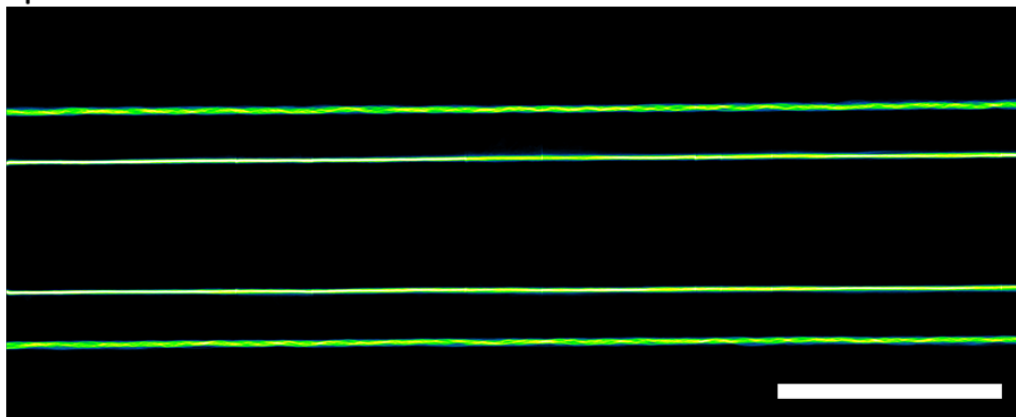
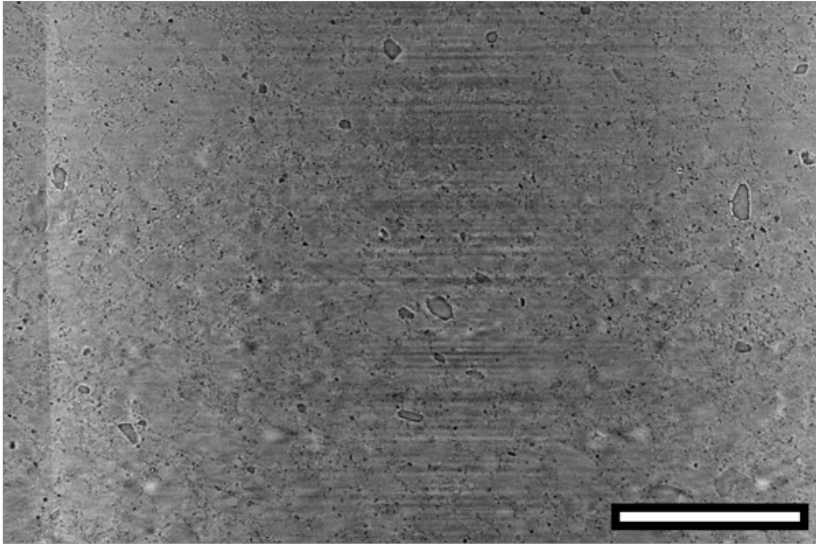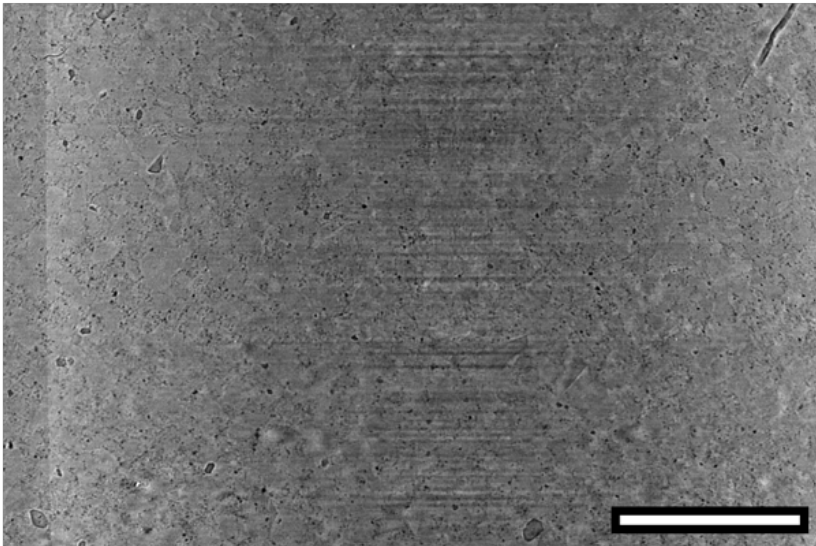**Supplementary Fig. 10** Cross-sectionally flattened 3D data (average) of the edge of the segmented electrodes at pristine, half cycle and full cycle
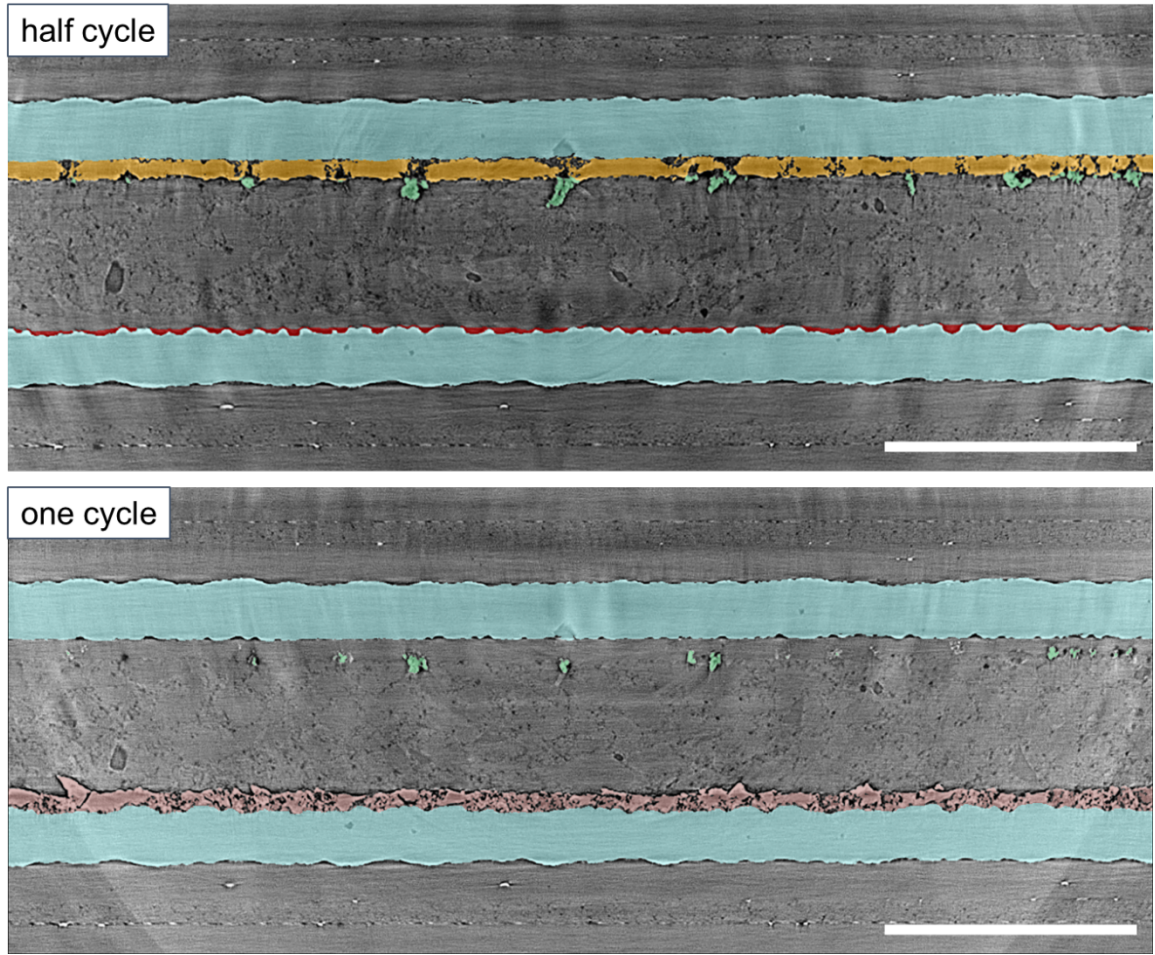
Supplementary Fig. 11 Representative in-plane images of the solid-state electrolyte region
Scale bar: 500 μm.

Supplementary Fig. 12 Examples of the final prediction of the U-Net model
Scale bar: 500 µm. Blue represents the electrodes. Yellow represents the deposited Li. Green represents the dendrites. Brown represents the redeposited Li.

Supplementary Table 1 Breakdown of per-class test set intersection-over-union (IoU) metric for final cross-sectional U-Net model. The test set consisted of 31 512x512 pixel patches randomly selected across 42 cross-sectional slice final hand label set.

Class	IoU
Dendrite	69.4%
Pit	86.5%
Deposited Li	78.8%
Electrode	97.0%
Total	95.5%

References

1   Lowekamp, B., Chen, D., Ibanez, L. & Blezek, D. The Design of SimpleITK. *Frontiers in Neuroinformatics* **7**, doi:10.3389/fninf.2013.00045 (2013).

2   Ronneberger, O., Fischer, P. & Brox, T. U-Net: Convolutional Networks for Biomedical Image Segmentation. *International Conference on Medical image computing and computer-assisted intervention.* 234-241 (Springer).

3   Innamorati, C., Ritschel, T., Weyrich, T. & Mitra, N. J. Learning on the edge: Explicit boundary handling in CNNs. *arXiv preprint arXiv:1805.03106* (2018).

4   Cui, Y., Zhang, G., Liu, Z., Xiong, Z. & Hu, J. A deep learning algorithm for one-step contour aware nuclei segmentation of histopathology images. *Medical & biological engineering & computing* **57**, 2027-2043 (2019).

5   Consortium, M. Project monai. *Zenodo. Available online: https://zenodo. org/record/4323059#. YXaMajgzaUk (accessed on 25 May 2020)* (2020).

6   Kerfoot, E. *et al.* in *International Workshop on Statistical Atlases and Computational Models of the Heart.* 371-380 (Springer).

7   He, K., Zhang, X., Ren, S. & Sun, J. in *European conference on computer vision.* 630-645 (Springer).

8   Schindelin, J. *et al.* Fiji: an open-source platform for biological-image analysis. *Nature Methods* **9**, 676-682, doi:10.1038/nmeth.2019 (2012).

9   *Coloc 2, <https://imagej.net/plugins/coloc-2> (2018).*